Archives of Civil and Mechanical Engineering (2022) 22:207
https://doi.org/10.1007/s43452-022-00522-5

ORIGINAL ARTICLE

Effect of annealing on the microstructure and properties of IN 625 specimens manufactured by selective laser melting

Ryszard Sitek[1] · Jakub Ciftci[1] · Dorota Moszczyńska[1] · Piotr Maj[1] · Ewa Ura-Bińczyk[1] · Piotr Warzybok[2] · Iwona Cieślik[2] · Paweł Wiśniewski[1] · Jarosław Mizera[1]

Received: 5 November 2021 / Revised: 1 August 2022 / Accepted: 5 August 2022 / Published online: 22 September 2022

Abstract
The study examines the effect of the annealing on the microstructure, tensile strength (small flat dog-bone specimen size with 5 mm dimension of measuring base) and corrosion resistance of IN 625 nickel superalloy specimens manufactured by means of selective laser melting method (SLM). The annealing of such specimens was carried out in a chamber furnace in a protective atmosphere of argon at a temperature of 1038 °C for 1 h. The cooling process was carried out in an atmosphere of air at ambient temperature. The microstructure of the IN 625 nickel superalloy after the 3D printing process and after the post-process heat treatment (HT) was examined by means of scanning electron microscopy (SEM) and electron backscatter diffraction (EBSD). The results showed a uniform microstructure after the SLM process with element microsegregation. The cooling rate in the heat treatment was not sufficient which caused precipitation at the grain boundaries, most probably carbides and resulted in only a partial increase in ductility much lower than that of the material in initial state despite the high temperature applied during the annealing. The strength in the HT was on a level comparable to as-build state, 852 MPa and 891 MPa, respectively. Additional corrosion resistance tests were performed by the potentiodynamic method in a 3.5% NaCl solution at room temperature. HT increased the current density variation from i_{pass} due to the formed precipitates. Our studies show that the size effect is an important factor when assessing the properties of IN 625 obtained using SLM. Despite similar microstructure, the structure defects play a more significant role which translates into lower mechanical properties than in normal sized specimens defined by the standard ASTM E8.

1 Introduction

Owing to its high creep, oxidation resistance, and good fatigue strength at high temperatures, IN 625 nickel superalloy is widely used in the aircraft industry for components of hot engines and ground-based gas turbines [1–4]. Apart from high temperature applications, IN 625 nickel superalloy is also used in low-temperature applications, such as in the chemical and shipbuilding industries, especially in sea installations, in which chlorides are present [5–7]. The high corrosion, good weldability, and high strength resistance is especially important in aggressive environments. Therefore, there is a large number of studies in which those

✉ Ryszard Sitek
ryszard.sitek@pw.edu.pl

Jakub Ciftci
jakub.ciftci.stud@pw.edu.pl

Dorota Moszczyńska
dorota.moszczynska@pw.edu.pl

Piotr Maj
Piotr.maj@pw.edu.pl

Ewa Ura-Bińczyk
ewa.ura@pw.edu.pl

Piotr Warzybok
Piotr.warzybok@gmail.com

Iwona Cieślik
Iwona.Cieslik@ncbj.gov.pl

Paweł Wiśniewski
pawel.wisniewski@pw.edu.pl

Jarosław Mizera
jaroslaw.mizera@pw.edu.pl

[1] Faculty of Materials Science and Engineering, Warsaw University of Technology, Wołoska 141 Str., 02-507 Warsaw, Poland

[2] National Centre for Nuclear Research, Andrzeja Sołtana 7, 05-400 Otwock-Świerk, Poland

particular properties are tested and analyzed especially for new manufacturing technologies [8–14].

The very high mechanical properties of IN 625 are mostly a result of solution and precipitation hardening [15, 16]. Phases present in the material include the fully coherent gamma prime, carbides, and intermetallic phases. Due to those microstructural barriers and crystal lattice resistance, the movement of dislocations may be significantly hampered [17]. The main elements improving the corrosion resistance of IN 625 nickel superalloy are molybdenum, niobium, and chromium. Molybdenum (Mo) improves the corrosion resistance of IN 625 nickel superalloy, niobium (Nb) counteracts intercrystalline corrosion owing to the formation of carbides in the form of precipitations, and chromium (Cr) increases the resistance to oxidation [18]. An important property of IN 625 nickel superalloy is its relatively good weldability compared with other nickel superalloys [19]. This feature makes components manufactured from IN 625 nickel superalloy powder using additive technologies the subject of studies at numerous scientific centers with regard to their implementation in various industrial branches [20–22]. The literature data [18] show that the segregation of niobium, which takes place during the material's crystallization during the solidification of the weld puddle—especially when high energy values are applied—causes an enrichment of the interdendritic areas with this element and a worsening of the corrosion properties of the superalloy. The formation of phases based on niobium, which increase the material's intercrystalline corrosion resistance, is possible owing to the use of post-process annealing [23, 24]. Corrosion resistance tests carried out on IN 740H nickel alloy in 0.1 M NaCl have showed that the corrosion processes in the material occur mainly at the grain boundaries [25]. Additionally, at room temperature, the corrosion resistance of IN 718 nickel alloy has been observed in aqueous environments containing chlorides [26]. Cabrini et al. [27] have demonstrated that parts of IN 625 manufactured by the selective laser melting method are resistant to pitting corrosion, both after the 3D printing process and after post-process annealing.

The scale/size effect, which has been analyzed in many works, is a combination of many factors that should be taken into account; these are divided into external (caused by specimen size) and internal (resulting from microstructural limitations) factors [28]. One of the external constraints is the fact that normal grain growth usually stagnates once the grain size becomes comparable to the thickness of the specimen [29]. Two common internal factors of the scale effect are the Hall–Petch effect (the dependence of grain size on strength) [30] and the influence of the grain size of secondary phases [31]. The biggest advantage of mini-specimens is that they make it possible to test the properties of a material, when its small volume is available [32]. However, Wysocki et al. [33] reported a lower elongation for additively manufactured commercially pure titanium, due to the scale effect and the variability of surface defects. The impact of surface preparation on the tensile properties obtained from mini-specimens was analyzed by Molak et al. [34] it was shown that thin layers of oxides from WEDM can reduce strength compared to the reference sample if the specimen thickness is below 0.5 mm. In the current research samples, a thickness of 0.6 mm were used and the effect was negligible.

Specimens produced by the SLM technique can feature defects in the form of microcracks and micropores, which reduce corrosion resistance [35]. The porosity of a "lack of fusion" type can worsen galvanic corrosion along the boundary between the remelted material and the non-remelted powder [36, 37]. Paulin et al. [38] have shown that, in the case of the mechanical properties of IN 625 nickel superalloy produced by additive technology, the porosity levels do not significantly worsen its tensile strength. During examination of fatigue crack propagation, this "lack of fusion" type of porosity hinders the speed of crack development due to the prolonged path of cracking (crack branching mechanism) [38].

Heat treatment strongly affects the properties of additively manufactured materials [39, 40]. Especially, cooling rates can influence precipitation phenomena. Tinoco et al. [41] analyzed the solidification of modified IN 625 under different cooling rates, and reported a larger amount of Laves phases in the rapidly cooled specimen just at the end of the solidification process compared with the specimen that was cooled down with the furnace to room temperature. According to the authors this indicates a dissolution process as a consequence of back diffusion in the samples with lower cooling rate which is beneficial in terms of mechanical properties. Li et al. [42]conducted research on the effects of annealing at three different annealing temperatures followed by cooling the furnace down to room temperature, and applied it to IN 625 manufactured by selective laser melting. In the as-built state, 100 nm precipitates rich in Nb and Mo were observed; these dissolved during annealing at 1150 °C. Li et al. [43] also annealed specimens of IN 625 for 1 h at 700 °C, 1000 °C, 1150 °C and applied cooling in air. They reported a lattice constant increase at 1000 °C caused by a large number of carbides precipitating. Additionally, they stated that at this temperature the strengthening elements are gradually dissolved into the matrix. Marchese et al. [44] studied the interaction of individual phases in a pure IN 625 and with an addition of TiC. The experiment involved standard solution annealing at 1150 °C for 2 h, followed by water quenching The aim of the heat treatment was to solubilize the material, triggering recrystallization, and grain growth. This is a standard treatment for the wrought IN 625 which as the authors pointed out is also viable for the 3D printed element.

The literature also suggests that the size of the specimens is of crucial importance, which is a well-known fact analyzed separately in many other research papers [28, 33, 34]. This is especially important in the case of 3D printed elements, which are more heterogenous than simple wrought materials [45]. This is a result of the complicated heat dissipation and segregation of elements. The overall trend is to achieve materials as similar as possible to wrought and cast materials. The simple tensile tests assume homogeneity and limited impact of the surface which is an exposed non-continuous area with higher energy prone to oxidation [46]. In the case of the mini-specimens, the results are more susceptible to defects such as stress concentrators, which are common in the case of 3D printed materials [33].

The main aim of this article is to analyze and compare the tensile and corrosion results obtained for 3D-printed SLM specimens, both as-built and after HT. Additionally, the impact of having a small specimen size (used in this work) is analyzed with regard to other research available in the literature [47, 48] providing some additional insights. Overall, our results showed that it is possible to achieve comparable mechanical strength, although ductility, which is proportional to elongation, is still lower due to the nature of the heterogeneity induced in the 3D printing method.

2 Experimental

2.1 Materials

To manufacture 35 × 25 × 10 mm specimens using the SLM method, MetcoAdd 625A powder was used, the chemical composition of which is presented in Table 1. The distribution of powder particle sizes was analyzed utilizing laser diffraction (Horiba LA-950 analyzer), and their shapes were observed using a Hitachi TM-1000 scanning electron microscope (SEM).

In the preliminary research test specimens with the dimensions of 10 × 10 × 10 mm were prepared by the selective laser method (SLM) in a Concept Laser Mlab R device equipped with a fiber laser with the power of 100 W. The smaller specimens were used for the optimization of the manufacturing parameters to obtain the best density at relatively low energy input which could overheat the material and induce excess amounts of thermal stresses. Other parameters that were also taken into account were geometric accuracy and surface roughness although the selection was done arbitrarily on a comparative basis between individual specimens. The specimens were produced with the use of double-sided scanning (Fig. 1), where the scanning lines for each consecutive layer were perpendicular to those of the previous layer (scanning line rotation of 90 degrees). For the first scanning, the energy density was 40 J/mm^3, with the following parameters: laser power *P*—36 W, laser velocity *V*—600 mm/s, distance between consecutive paths *H*—0.05 mm, layer thickness *D*—0.03 mm, while for the second scanning, the energy density was 100 J/mm^3 with the parameters: *P*—90 W, *V*—600 mm/s, *H*—0.05 mm, *D*—0.03 mm.

For annealing, the conditions recommended by the powder manufacturer were applied. It was carried out in a chamber furnace, in a protective atmosphere of argon at 1038 °C (1900 °F) for 1 h. The heat treatment parameters were selected based on the standard procedures used by Oerlikon in a research report [49], where the authors specified them for 3D-printed IN 625. The specimen cooling process was carried out in air at ambient temperature.

2.2 Characteristics of the produced specimens

The microsections for the tests of the cubic specimens with a side length of 5 mm, were cut out using wire electro-discharge machining (WEDM) Mitsubishi MV-1200S. The following parameters were used in the process: current density—10 A, wire feed—5 m/min, wire tension—8 N Pulse on/off time—110/50 µs, respectively. The next step involved the use of abrasive papers with gradations of 320, 600, and 1200, and polished using diamond suspensions with

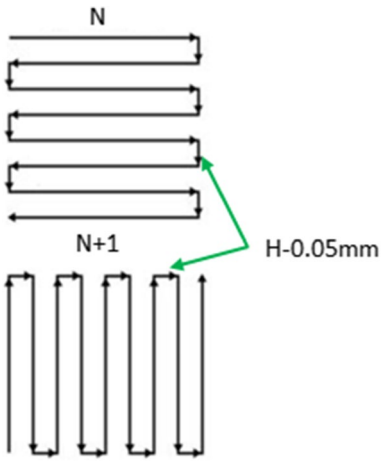

Fig. 1 Diagram of the specimen printing strategy

Table 1 Chemical composition of the MetcoAdd 625A powder

Element	Ni	Cr	Mo	Fe	Nb	Mn	Al	Ti	Co	P	Si	S	C
% wt	Balance	20–23	8–10	5.0 max	3.5–4.14	0.50 max	0.40 max	0.40 max	1.0 max	0.015 max	0.50 max	0.015 max	0.10 max

gradations of 3 µm, and then 1 µm. A preliminary study showed a heat-affected zone (HAZ) of up to 10 µm, which is negligible compared with the thickness of the specimen (0.6 mm). Furthermore, the thin layer of the HAZ served as a marker for the DIC method (described later in the text). The specimens for the microstructural observations were etched electrochemically using a mixture of 78 ml $HClO_4$, 100 ml $C_6H_{14}O_2$, 730 ml C_2H_5OH and 90 ml H_2O, at a voltage of 2 V for 30 s. The specimen microstructure observations were carried out on HITACHI SU 70 and HITACHI TM-1000 scanning electron microscopes. A detailed microstructure investigation was performed on a (SEM) Hitachi SU-70 scanning electron microscope equipped with an electron backscatter diffraction (EBSD) detector. A Hitachi ion milling system IM4000 was used to prepare the specimens for EBSD. Phase identification of the manufactured specimens was conducted using a Bruker D8 Advance X-ray diffractometer having filtered Cu Kα ($\lambda = 0.154056$ nm) radiation and operated at 40 kV and 40 mA. Bruker EVA software and a PDF-2 database were used to analyze the X-ray diffraction (XRD) patterns. The measurement conditions were as follows: the 2θ range was 20°–100°, the step 0.05, and sampling time 3 s per step.

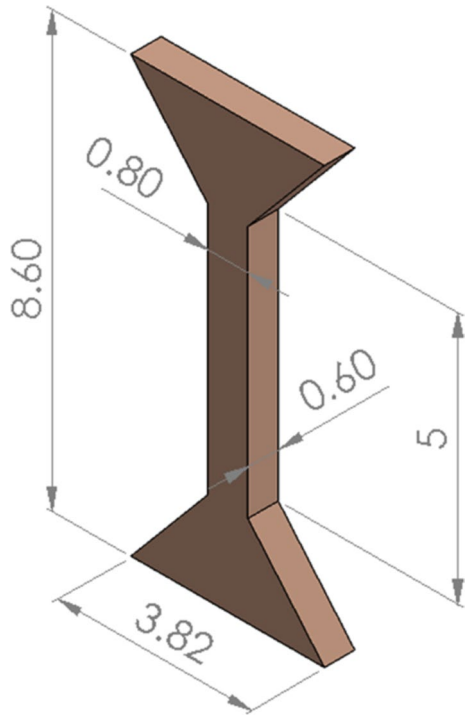

Fig. 2 Shape and dimensions of the miniature specimens for the static tensile test

2.3 Electrochemical testing

The electrochemical measurements were performed with the use of an Autolab PGSTAT302N potentiostat/galvanostat in a naturally aerated 3.5% NaCl solution. A standard three-electrode setup with a platinum sheet as the counter electrode (CE), a silver chloride electrode ($Ag|AgCl|Cl^-$) as the reference electrode (RE) and a specimen as the working electrode (WE) was used. The open circuit potential (E_{OCP}) was recorded during the 30 min of immersion. After E_{OCP} stabilization, the potentiodynamic polarization was started 0.15 V below E_{OCP} with a 1 mV/s scan rate, and reversed when the current density reached the value of 1 mA/cm^2. Each measurement was repeated at least 3 times to ensure the reproducibility of the results.

2.4 Static tensile test

A static tensile test was performed on mini-specimens with a length of 8.60 mm, cut out using EDM (Fig. 2). It should be noted that the specimen thickness was about 20 layers thick, and its width approximately the width of 16 melt lines with a hatch spacing of 0.05 mm. The test specimens were cut out in such a way so that their longer axis would be within the printing plane (xy) or (xz).

The static tensile test was carried out by means of a Zwick/Roell Z005 testing machine equipped with a power detector, with a measurement scope of ± 1 kN. The static tensile test was controlled by a time-constant shift of the tester beam of 0.005 mm/s, which, with the mini-specimen measuring base of 5 mm, ensured an initial absolute tensile speed of 1×10^{-1} 1/s. Due to the small size of the mini-specimens, for the deformation measurements a non-contact optical method based on digital image correlation (DIC) was applied. The idea of this method is based on a comparison of digital images of the specimen surface before the test (the so-called reference image) with images taken after deformation. A computer algorithm compares the particular photographs and calculates the shifts of small areas. Based on the measured shifts of the analyzed areas, it is possible to determine the macroscopic deformations, the local deformations, and the deformation fields over the whole analyzed specimen surface. In the tests, VIC 2d commercial software by Correlated Solutions was used to make two-dimensional deformation measurements on the specimen surface. An analysis of the static tensile test results (force [N]/stress [MPa]) as well as the DIC analyzes (deformation %) made it possible to produce an engineering stress-engineering strain relation and to determine the mechanical properties of the IN 625 nickel superalloy specimens in their initial state, as manufactured using the SLM technique, and after being subjected to additional post-process annealing. To obtain statistically significant results, a minimum of three specimens per state was used. In the case of significantly different results in the as-built state, a total of five specimens were used and extreme values were ignored.

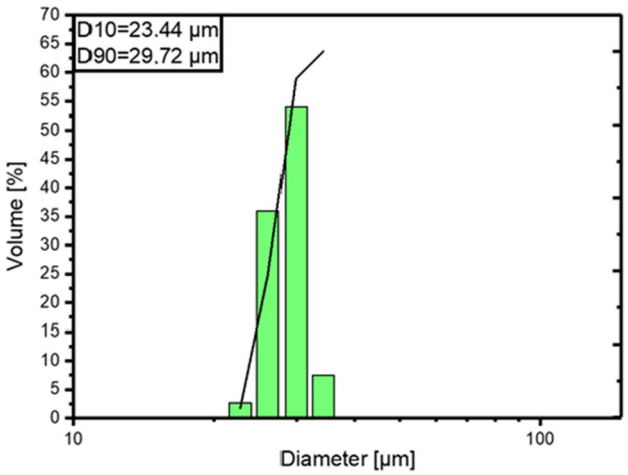

Fig. 3 Particle size distribution

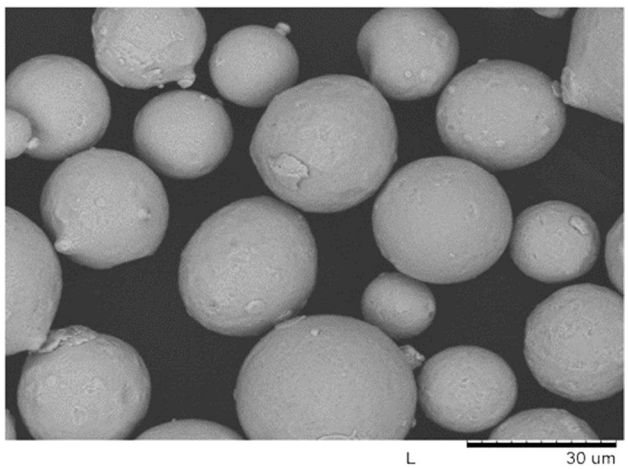

Fig. 4 Micrograph of the IN 625 powder (SEM BSE)

3 Results and discussion

3.1 Characteristics of the powder

Figure 3 shows a histogram of the particle size distribution of the IN 625 nickel superalloy powder. The histogram of the particle size distribution points to a narrow size scope, which is confirmed by the microscopic observations (Fig. 4).

The powder particles are spherical in shape, and their mean size is about 45 µm. The size of the powder particles, as well as their shape, are typical for additive manufacturing techniques.

3.2 Microstructure

3.2.1 SEM observations of as-printed SLM specimens

The microstructure imaging results of the specimens made from the IN 625 nickel superalloy powder using the SLM technique in the *x*–*y* plane are shown in Fig. 5. The microstructure observations performed by means of a scanning electron microscope (Fig. 5a) revealed padding weld beads arranged alternately, which was caused by the deposition of consecutive layers of the powder and the direction of the powder being melted by the laser beam. The differences in the padding weld bead sizes result from the difference in the sizes of the welded powder particles. The microstructure observations in the printing plane (*xz*) (Fig. 5b) revealed the melt pools, and a fine-grained microstructure containing dendrites. The dimensions of the melted pools of the IN 625 nickel superalloy were about 70–90 µm in width and about 20–45 µm in depth. The observed shape and size of the melted material puddles depended on the laser scanning pattern and was characteristic for nickel superalloy specimens produced using SLM/DMLS methods [50, 51].

3.2.2 SEM observations of heat-treated SLM specimens

Figure 6a and b show the microstructure of specimens produced by the SLM technique and subjected to additional annealing. We can see grains with a size of about 20 µm, as well as precipitations on the grain boundaries. The results of the chemical composition analysis (EDS) presented in Table 2 point to an enrichment of the precipitations with Nb and Mo, and to an impoverishment in those areas of Ni and Cr compared with the above-mentioned grains. Furthermore higher concentration of carbon in those areas allows to suggest the presence of carbides.

3.2.3 Electron backscatter diffraction (EBSD)

Figure 7 shows inverse pole figure (IPF) maps of the XZ cross-sections for the as-SLM and heat-treated specimens. The IPF map is color-coded to identify the crystallographic orientations on a standard stereographic projection. In both of the examined specimens (SLM-obtained and heat-treated), the equiaxial grains have a strong $<001>$ orientation along the manufacturing direction. The annealing performed increased the mean subgrain diameter (d) by more than 50%. The increase in the distribution of high angle grain boundaries (HAGB) was also on a comparable level in the state after the annealing.

The X-ray diffraction (XRD) patterns of the SLM (XY) and heat-treated (XYHT) specimens are shown in Fig. 8. A nickel-based solid solution (γ-Ni) with an FCC crystal structure was detected in all the examined specimens. As shown

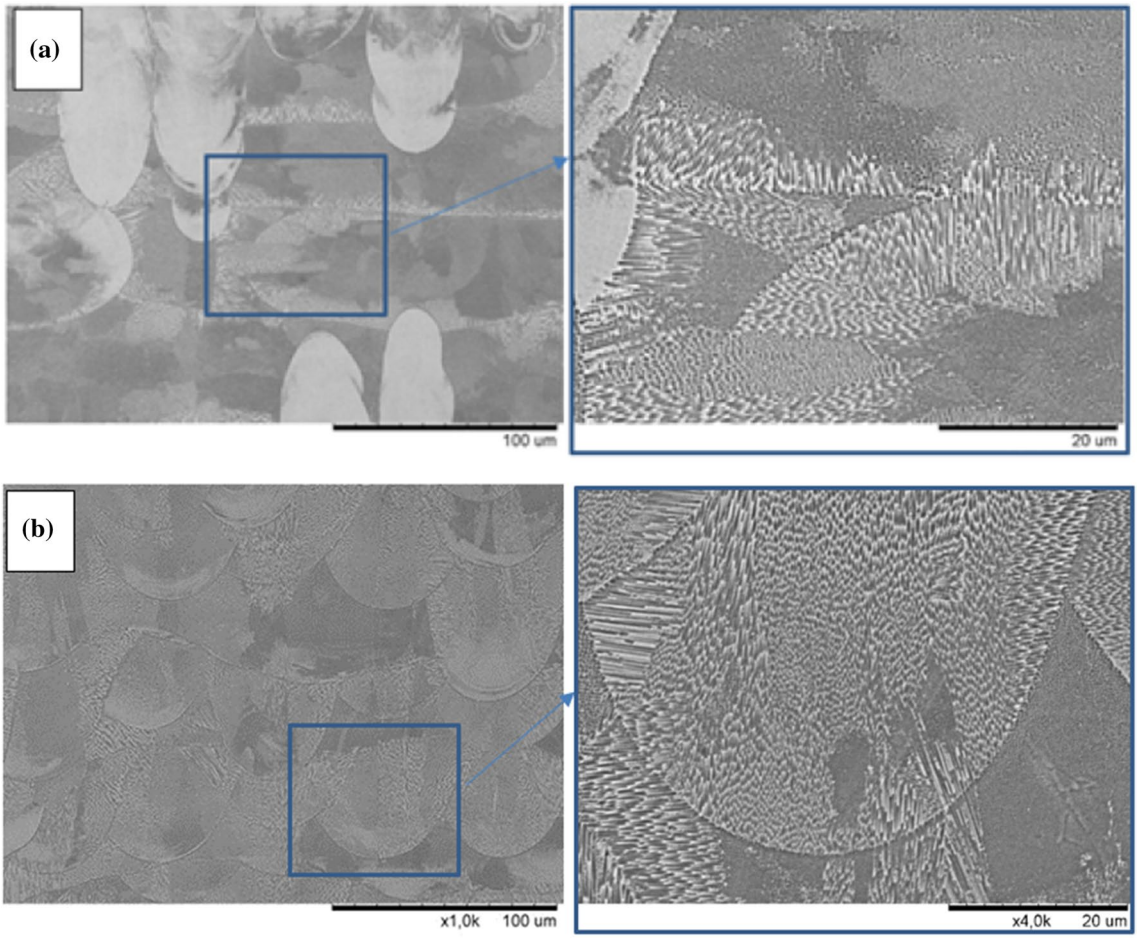

Fig. 5 Microstructure of a specimen produced using SLM: in the printing plane (*XY*) (**a**) and (*XZ*) (**b**), (SEM BSE)

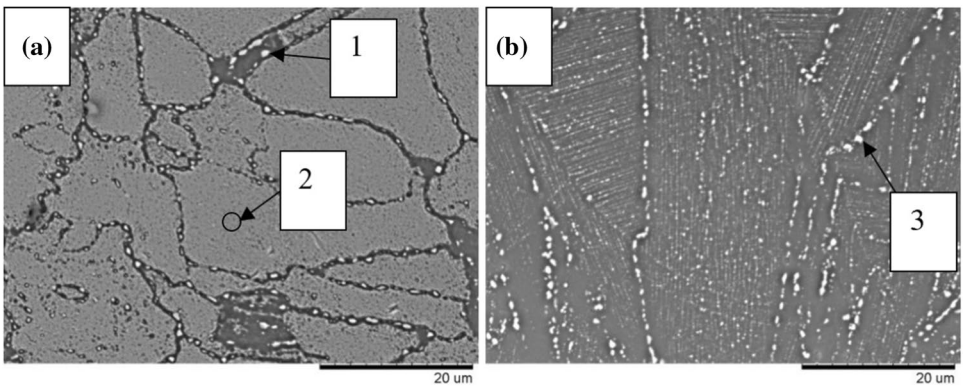

Fig. 6 Microstructure of IN 625 nickel alloy specimens made using the SLM technique and subjected to additional annealing: in the printing plane (*XY*) (**A**), in the printing plane (*XZ*) (**B**)

in the magnified area, the peak corresponds to the (111) plane shifted to a lower diffraction angle after the annealing. This displacement in the XRD peak position may be due to a variation in the lattice parameter of the γ-Ni structure. In light of the work of Amato et al. [52], the intermetallic γ″ (Ni_3Nb) particles found in the NiCr matrix in the as-SLM state dissolved into the matrix after the heat treatment.

3.3 Pitting corrosion

The potentiodynamic polarization curves, recorded after 0.5 h of stabilization at the open circuit potential (E_{OCP}) in 3.5% NaCl, are plotted in Fig. 9. The wide passive plateau on the potentiodynamic curves indicates that heat in the test solution. The shapes of all the curves were very

Table 2 Results of a quantitative chemical composition analysis in the precipitations and the substrate of IN 625 nickel superalloy specimens produced using SLM technique and subjected to additional heat treatment [% wt.]

Measurement point	C	Al	Si	Cr	Fe	Ni	Ti	Co	Nb	Mo
1	1.8	0.2	0.5	14.9	3.6	33.5	2.4	0.3	25.1	17.7
2	0.7	0.4	0.3	21.5	3.7	58.8	0.3	0.8	3.7	9.8
3	2.3	0.3	0.4	13.1	3.8	39.3	1.8	0.1	23.5	15.4

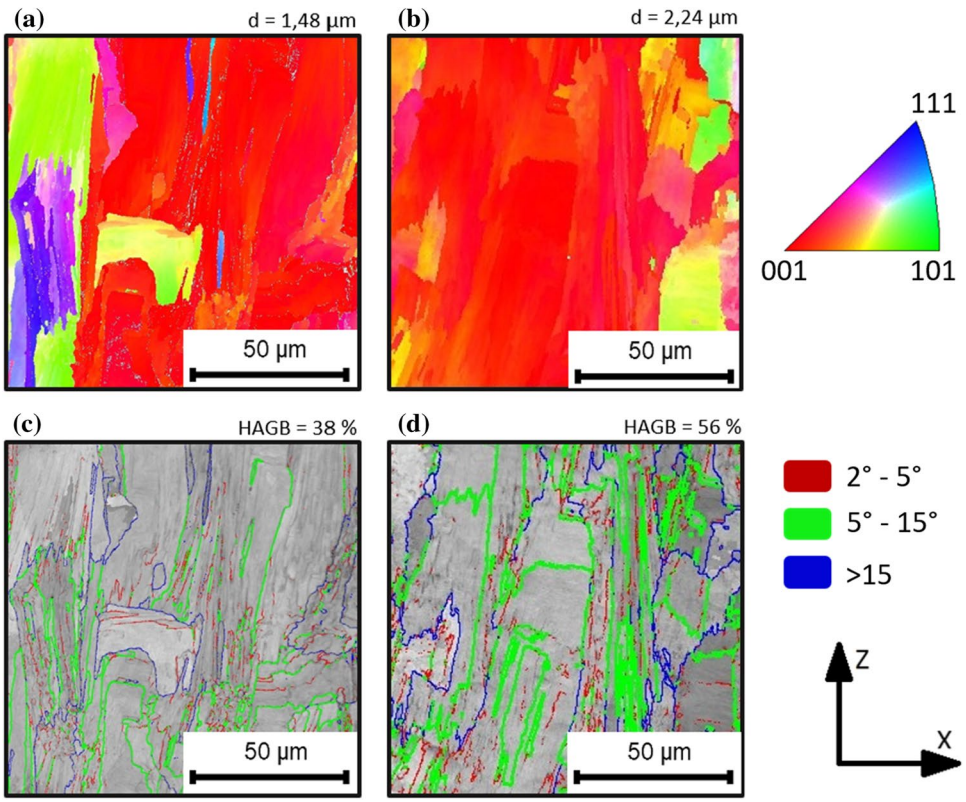

Fig. 7 EBSD maps of SLM (**A**) and heat-treated specimens (**B**)

similar (Fig. 9a), the corrosion potential (E_{corr}) values were equal to about ~ 0.18 V/Ref and the passive current densities (i_{pass}) were in a range of 3–5 µA/cm^2. The major difference between the potentiodynamic curves were the current spikes observed in the passive domain for the heat-treated specimens (Fig. 9b). A sudden growth in current density followed by the abrupt drop down to i_{pass} was observed multiple times for the XY_HT and XZ_HT specimens. Such a phenomenon is related to a local dissolution of the material followed by its repassivation [53]. The microstructural observations revealed the formation of Nb- and Mo-rich phase at the grain boundaries. The galvanic coupling between that phase and the surrounding matrix might lead to a local dissolution and repassivation of the passive film. At potential of about 0.8 V/Ref, the increase in the current density was related to the oxygen evolution reaction. In the reverse scan, the current density quickly decreased below the values recorded in the forward scan, which indicated that no stable pitting had occurred. The heat treatment of the SLM specimens did not significantly alter the resistance against localized corrosion attack. However, the occurrence of local dissolution events might indicate that the formation of Nb-, Mo-rich precipitates at the grain boundaries led to the formation of a less compact and less stable passive film.

3.4 Static tensile test

Figure 10 shows the tensile curves obtained for IN 625 superalloy specimens produced by the SLM technique before and after annealing. The mechanical properties determined from the tensile curves are included in Table 3. On the basis of the compiled investigation results, it can be established that, after the SLM process, the IN 625 superalloy features good strength parameters, which are not much lower than

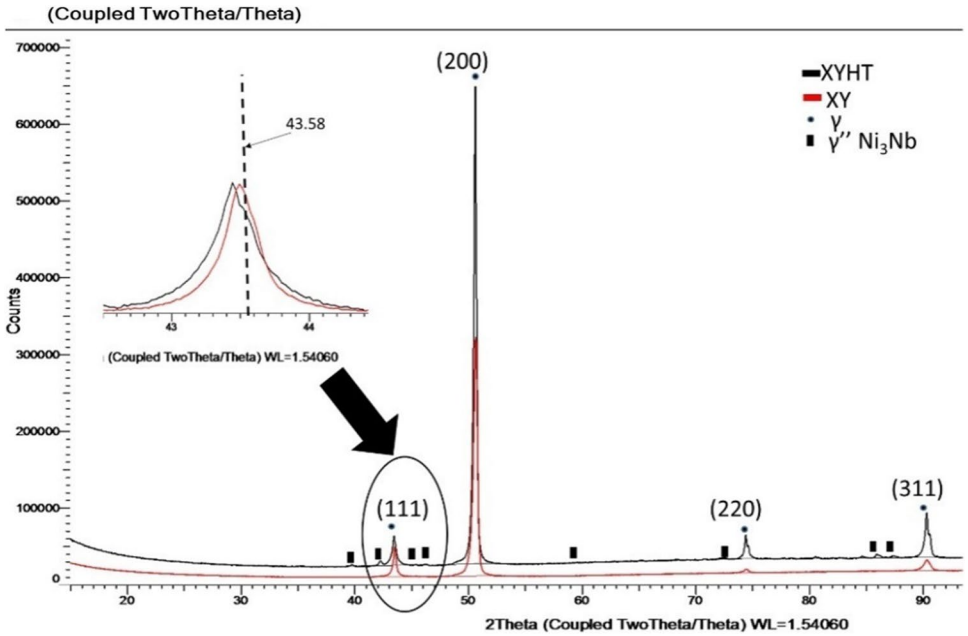

Fig. 8 XRD patterns of the SLM (*XY*) and heat treated (*XY* HT) specimens with the magnified view of the (111) crystal plane

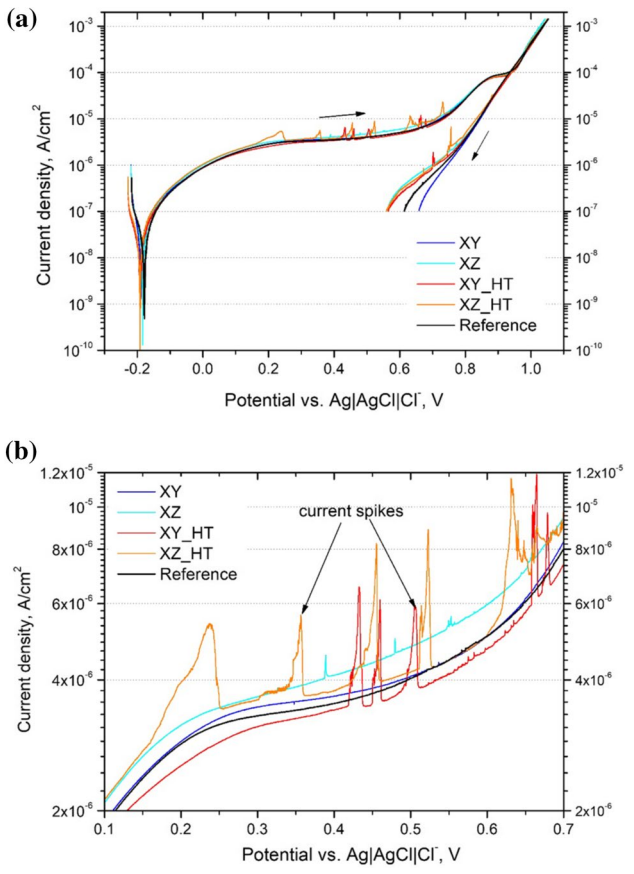

Fig. 9 Anodic potentiodynamic polarization curves (**a**) and enlarged passive domain potential range (**b**) recorded in 3.5% NaCl for the XY, XZ, XY_HT, XZ_HT and reference specimens

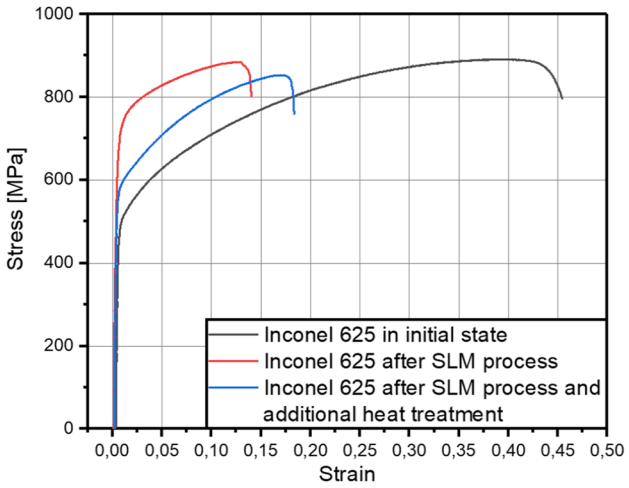

Fig. 10 Curves in the stress–strain results obtained for IN 625: wrought material, after SLM process and after SLM process with additional heat treatment

those of the IN 625 nickel superalloy specimens in the initial state ($Rp_{0.2} = 502$ MPa, $R_m = 891$ MPa, $A = 44\%$); this indicates that the technological parameters of the SLM process were correctly elaborated. The biggest differences were recorded in the values of elongation at break, which have resulted from the presence of pores in the superalloy. The pores decreased the actual cross-section of the specimen and constituted structural notches which, in consequence, significantly reduced the material's plasticity. The annealing did not significantly affect the strength properties of the IN 625 nickel alloy. However, the value of elongation at break, which was 15% for the SLM process and 19% for the

Table 3 Comparison of literature data and results obtained from the tensile tests conducted on the mini-specimens

Material condition	Applied HT (temperature/time/cooling method)	YS [MPa]	UTS [MPa]	*A* [%]	Described microstructure elements	Sources
As-built	–	783 ± 23	1041 ± 36	33 ± 1	Cellular and columnar dendritic structures Nb-rich MC carbides	[47]
Heat-treated	1150 °C/2 h/WQ	396 ± 9	883 ± 15	55 ± 1	Recrystallized γ grains Nb, Ti–rich MC carbides Intergranular secondary carbides	[47]
As-built	–	619 ± 7	901 ± 10	56.7 ± 2	–	[47]
Heat-treated	1048 °C/1 h/ FC	523 ± 4	841 ± 7	68.5 ± 2	Columnar grains	[54]
As-built	–	618 ± 33	891 ± 5	40.7 ± 0.5	Cellular and columnar dendritic structures	[55]
Heat-treated	1150 °C/2 h/ WQ	379 ± 9	851 ± 3	54.5 ± 1.1	Equiaxed grains Sub-micrometric carbides	[55]
Heat-treated	1150 °C/2 h/WQ and 900 °C/200 h/–	450 ± 8	920 ± 4	46 ± 1.5	γ phase δ phase	[48]
As-built	–	652 ± 10	925 ± 13	32 ± 3	Cellular-shaped structure Primary dendrites	[56]
Heat-treated	900 °C/1 h/AC	567 ± 15	869 ± 7	38 ± 1	Elongated grains	[56]
Heat-treated	1100 °C/1 h/AC	409 ± 14	886 ± 11	56 ± 5	Elongated grains Annealing twins;	[56]
As-built	–	567 ± 15	836 ± 17	45.2 ± 1.1	Dendritic cellular structure and columnar structure Laves phases MC carbides	[57]
Heat-treated	1070 °C/1 h/WQ and 720 °C/18 h/–	813 ± 11	927 ± 15	43 ± 0.6	Annealing twins Equiaxed grains Recrystallized grains MC carbides disk-shaped γ″ phase	[57]
As-built	–	669 ± 21	855 ± 32	15 ± 1	Fine-grained microstructure containing dendrites	This work
Heat-treated	1038 °C/1 h/AC	577 ± 2	854 ± 5	19 ± 1	Nb, Mo-rich precipitations on grain boundaries	This work
Wrought	–	483 ± 18	881 ± 9	36 ± 8		This work

YS yield strength, *UTS* ultimate tensile strength, *A* elongation to failure, *WQ* water quenching, *FC* furnace cooling, *AC* air cooled

SLM process and the annealing, did not limit the potential construction applications of the IN 625 material produced using the SLM method.

Figure 11 shows the fracture surfaces after the tensile tests. IN 625 in the initial state had the characteristics of a ductile fracture surface (Fig. 11a). It was found that the fracture of the IN 625 superalloy after the SLM process had the features of a plastic (ductile) fracture (Fig. 11b). The pores visible in the cross-section are structural notches that limit the ductile properties of the material to a small extent. The fracture of the specimen after additional annealing (Fig. 11c) is similar to the fracture of the specimen after the SLM process. It is a ductile fracture with visible pores. The lower plasticity of specimens after the SLM process (in the as-built state) than that reported in [40] was due to usage of different specimen size. In our work, we used mini-specimens, whereas Marchese et al. [47] conducted their research on cylindrical specimens under the ASTM E8/E8M-09 standards. Mini-specimens are known for higher sensitivity for material failure initiators. According to the research conducted, there are many challenges posed by the precise 3D printing of small parts. In this study, the size effect proved critical when assessing the mechanical and environmental response of the material. Despite the use of the same material (SLM printed IN 625), the results showed a large spread due to small defects and the larger share of grain boundaries, which were additionally affected by the annealing and Cr, Nb and Mo segregation. Furthermore, small pores were the precursors for fracture in the tensile tests. It should be noted

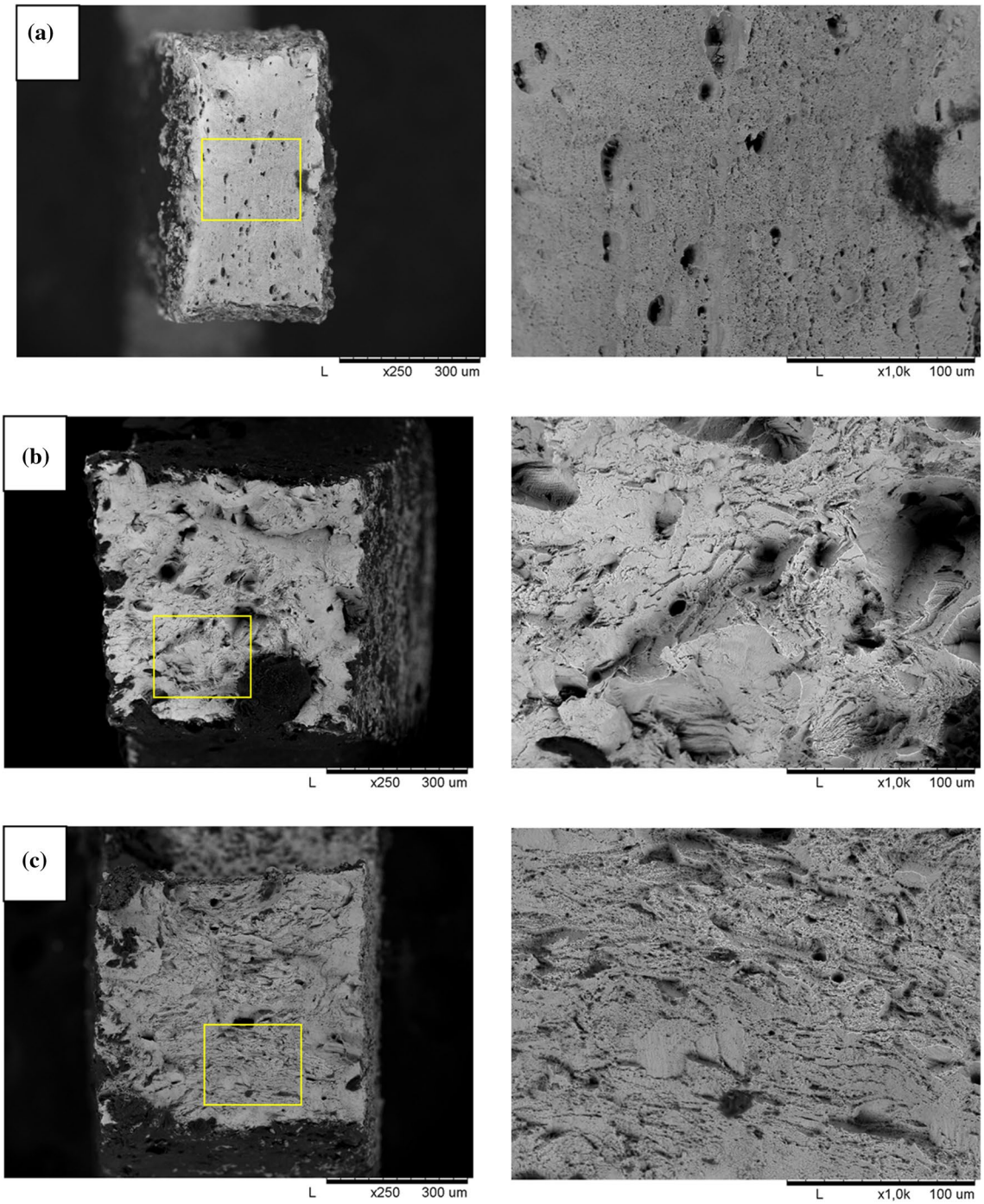

Fig. 11 Fractography of tested specimens of IN 625: in initial state (**a**); after the SLM process (**b**); after the SLM process and additional heat treatment (**c**)

that the results of microstructure observations were in line with other similar studies [23, 57] yet the elongation was significantly lower. This proves overall that, depending on the size and usage, separate tests should be done for small parts, since these display different characteristics than the bulk solid material.

4 Conclusions

Based on an analysis of the results of our investigation, the following conclusions have been drawn:

1. The SLM technique can be used to manufacture IN 625 nickel superalloy powder specimens with a directed, fine-crystalline microstructure containing carbides and the Ni_3Nb phase.
2. The IN 625 nickel superalloy specimens, manufactured by selective laser melting (SLM) under the optimized parameters, exhibit corrosion resistance and tensile strength, which are comparable with the specimens of the wrought alloy. At the same time, elongation of the 3D printed specimens was remarkably lower because of carbide phase precipitation and structural defects.
3. Decrease in the size of the SLM specimens led to worsening of the mechanical properties of the alloy.

Acknowledgements This scientific research was financed from statutory work No.504/04208/1090/44.000000.

Declarations

Ethical approval This article does not contain any studies with human participants or animals performed by any of the authors.

References

1. Maj P, Koralnik M, Adamczyk-Cieslak B, Romelczyk-Baishya B, Kut S, Pieja T, Mrugala T, Mizera J. Mechanical properties and microstructure of Inconel 625 cylinders used in aerospace industry subjected to flow forming with laser and standard heat treatment. Int J Mater Form. 2019;12:135–44. https://doi.org/10.1007/s12289-018-1413-8.
2. Yadav M, Misra A, Malhotra A, Kumar N. Design and analysis of a high-pressure turbine blade in a jet engine using advanced materials. Mater Today Proc. 2020;25:639–45. https://doi.org/10.1016/j.matpr.2019.07.530.
3. Eiselstein HL, Tillack DJ. The invention and definition of alloy 625. In: Loria EA (ed) Superalloys 718, 625 Var. Deriv., TMS, 1991: pp. 1–14.
4. Mostafaei A, Stevens EL, Hughes ET, Biery SD, Hilla C, Chmielus M. Powder bed binder jet printed alloy 625: densification, microstructure and mechanical properties. Mater Des. 2016;108:126–35. https://doi.org/10.1016/j.matdes.2016.06.067.
5. Floreen S, Fuchs G, Yang WJ. The metallurgy of alloy-625. In: Loria EA (ed) Superalloys 718, 625 Var. Deriv., TMS, 1994; pp 13–37.
6. Shoemaker LW. Alloys 625 and 718: trends in properties and applications. In: Loria EA (ed) Superalloys 718, 625, 706 Deriv., TMS, 2005: pp. 409–418.
7. Ban S. Corrosion resistance of Inconel 625 overlay welded inside pipes as a function of heat treatment temperature. Int J Electrochem Sci. 2016;11:7764–74. https://doi.org/10.20964/2016.09.22.
8. Łyczkowska K, Michalska J. Studies on the corrosion resistance of laser-welded Inconel 600 and Inconel 625 nickel-based superalloys. Arch Metall Mater. 2017;62:653–6. https://doi.org/10.1515/amm-2017-0100.
9. de Lorenzi MS, Nunes RM, Falcade T, Clarke T. Evaluation of the influence of surface finishing on the corrosion resistance of HVOF applied Inconel 625 coatings on steel. Mater Res. 2017. https://doi.org/10.1590/1980-5373-mr-2016-0844.
10. Xu LY, Li M, Jing HY, Han YD. Electrochemical behavior of corrosion resistance of X65/Inconel 625 welded joints. Int J Electrochem Sci 2013;8:2069–2079. www.electrochemsci.org accessed 26 Apr 2022.
11. Koike R, Unotoro I, Kakinuma Y, Aoyama T, Oda Y, Kuriya T, Fujishima M. Evaluation for mechanical characteristics of Inconel625–SUS316L joint produced with direct energy deposition. Procedia Manuf. 2017;14:105–10. https://doi.org/10.1016/j.promfg.2017.11.012.
12. Park I-C, Kim S-J. Corrosion behavior in seawater of arc thermal sprayed Inconel 625 coatings with sealing treatment. Surf Coat Technol. 2017;325:729–37. https://doi.org/10.1016/j.surfcoat.2017.03.009.
13. Gamon A, Arrieta E, Gradl PR, Katsarelis C, Murr LE, Wicker RB, Medina F. Microstructure and hardness comparison of as-built inconel 625 alloy following various additive manufacturing processes. Results Mater. 2021;12: 100239. https://doi.org/10.1016/j.rinma.2021.100239.
14. Marchese G, Parizia S, Rashidi M, Saboori A, Manfredi D, Ugues D, Lombardi M, Hryha E, Biamino S. The role of texturing and microstructure evolution on the tensile behavior of heat-treated Inconel 625 produced via laser powder bed fusion. Mater Sci Eng A. 2020;769: 138500. https://doi.org/10.1016/j.msea.2019.138500.
15. Liu X, Fan J, Li K, Song Y, Liu D, Yuan R, Wang J, Tang B, Kou H, Li J. Serrated flow behavior and microstructure evolution of Inconel 625 superalloy during plane-strain compression with different strain rates. J Alloys Compd. 2021;881: 160648. https://doi.org/10.1016/j.jallcom.2021.160648.
16. Zhang YC, Jiang W, Tu ST, Zhang XC, Ye YJ, Wang RZ. Experimental investigation and numerical prediction on creep crack growth behavior of the solution treated Inconel 625 superalloy. Eng Fract Mech. 2018;199:327–42. https://doi.org/10.1016/j.engfracmech.2018.05.048.
17. Reed RC. The superalloys : fundamentals and applications. Cambridge University Press; 2006.
18. Alvarães CP, Jorge JCF, de Souza LFG, Araújo LS, Mendes MC, Farneze HN. Microstructure and corrosion properties of single layer Inconel 625 weld cladding obtained by the electroslag welding process. J Mater Res Technol. 2020;9:16146–58. https://doi.org/10.1016/j.jmrt.2020.11.048.
19. Henderson MB, Arrell D, Larsson R, Heobel M, Marchant G. Nickel based superalloy welding practices for industrial gas turbine applications. Sci Technol Weld Join. 2004;9:13–21. https://doi.org/10.1179/136217104225017099.

20. Kreitcberg A, Brailovski V, Turenne S. Effect of heat treatment and hot isostatic pressing on the microstructure and mechanical properties of Inconel 625 alloy processed by laser powder bed fusion. Mater Sci Eng A. 2017;689:1–10. https://doi.org/10.1016/j.msea.2017.02.038.
21. Beese AM, Wang Z, Stoica AD, Ma D. Absence of dynamic strain aging in an additively manufactured nickel-base superalloy. Nat Commun. 2018;9:2083. https://doi.org/10.1038/s41467-018-04473-5.
22. Li X, Yi D, Liu B, Zhang J, Yang X, Wang C, Feng Y, Bai P, Liu Y, Qian M. Graphene-strengthened Inconel 625 alloy fabricated by selective laser melting. Mater Sci Eng A. 2020;798: 140099. https://doi.org/10.1016/j.msea.2020.140099.
23. Tian Z, Zhang C, Wang D, Liu W, Fang X, Wellmann D, Zhao Y, Tian Y. A review on laser powder bed fusion of inconel 625 nickel-based alloy. Appl Sci. 2020;10:81. https://doi.org/10.3390/app10010081.
24. Smith GD, Eisinger NC. The effect of niobium on the corrosion resistance of nickel - base alloys. In: Kim Y-W, Carneiro T (eds) Niobium high temp. Appl., TMS, 2004: pp. 23–34.
25. Sitek R, Kaminski J, Mizera J. Corrosion resistance of the inconel 740H nickel alloy after pulse plasma nitriding at a frequency of 10 kHz. Acta Phys Pol A. 2016;129:584–7. https://doi.org/10.12693/APhysPolA.129.584.
26. Huang CA, Wang TH, Han WC, Lee CH. A study of the galvanic corrosion behavior of Inconel 718 after electron beam welding. Mater Chem Phys. 2007;104:293–300. https://doi.org/10.1016/j.matchemphys.2007.03.017.
27. Cabrini M, Lorenzi S, Testa C, Pastore T, Brevi F, Biamino S, Fino P, Manfredi D, Marchese G, Calignano F, Scenini F. Evaluation of corrosion resistance of alloy 625 obtained by laser powder bed fusion. J Electrochem Soc. 2019;166:C3399–408. https://doi.org/10.1149/2.0471911jes.
28. Arzt E. Size effects in materials due to microstructural and dimensional constraints: a comparative review. Acta Mater. 1998;46:5611–26. https://doi.org/10.1016/S1359-6454(98)00231-6.
29. Mullins W. The effect of thermal grooving on grain boundary motion. Acta Metall. 1958;6:414–27. https://doi.org/10.1016/0001-6160(58)90020-8.
30. Dunstan DJ, Bushby AJ. Grain size dependence of the strength of metals: the Hall-Petch effect does not scale as the inverse square root of grain size. Int J Plast. 2014;53:56–65. https://doi.org/10.1016/j.ijplas.2013.07.004.
31. Tucho WM, Hansen V. Characterization of SLM-fabricated Inconel 718 after solid solution and precipitation hardening heat treatments. J Mater Sci. 2019;54:823–39. https://doi.org/10.1007/s10853-018-2851-x.
32. Molak RM, Paradowski K, Brynk T, Ciupinski L, Pakiela Z, Kurzydlowski KJ. Measurement of mechanical properties in a 316L stainless steel welded joint. Int J Press Vessel Pip. 2009;86:43–7. https://doi.org/10.1016/j.ijpvp.2008.11.002.
33. Wysocki B, Maj P, Krawczyńska A, Rożniatowski K, Zdunek J, Kurzydłowski KJ, Święszkowski W. Microstructure and mechanical properties investigation of CP titanium processed by selective laser melting (SLM). J Mater Process Technol. 2017;241:13–23. https://doi.org/10.1016/j.jmatprotec.2016.10.022.
34. Molak RM, Kartal ME, Pakiela Z, Kurzydlowski KJ. The effect of specimen size and surface conditions on the local mechanical properties of 14MoV6 ferritic–pearlitic steel. Mater Sci Eng A. 2016;651:810–21. https://doi.org/10.1016/j.msea.2015.11.037.
35. Duan Z, Man C, Dong C, Cui Z, Kong D, Wang L, Wang X. Pitting behavior of SLM 316L stainless steel exposed to chloride environments with different aggressiveness: pitting mechanism induced by gas pores. Corros Sci. 2020;167: 108520. https://doi.org/10.1016/j.corsci.2020.108520.
36. Chen T-C, Chou C-C, Yung T-Y, Cai R-F, Huang J-Y, Yang Y-C. A comparative study on the tribological behavior of various thermally sprayed Inconel 625 coatings in a saline solution and deionized water. Surf Coatings Technol. 2020;385: 125442. https://doi.org/10.1016/j.surfcoat.2020.125442.
37. Tang M, Pistorius PC, Beuth JL. Prediction of lack-of-fusion porosity for powder bed fusion. Addit Manuf. 2017;14:39–48. https://doi.org/10.1016/j.addma.2016.12.001.
38. Poulin J-R, Kreitcberg A, Terriault P, Brailovski V. Long fatigue crack propagation behavior of laser powder bed-fused inconel 625 with intentionally-seeded porosity. Int J Fatigue. 2019;127:144–56. https://doi.org/10.1016/j.ijfatigue.2019.06.008.
39. Junker D, Hentschel O, Schmidt M, Merklein M. Investigation of heat treatment strategies for additively-manufactured tools of X37CrMoV5-1. Metals (Basel). 2018;8:1–13. https://doi.org/10.3390/met8100854.
40. Popovich VA, Borisov EV, Popovich AA, Sufiiarov VS, Masaylo DV, Alzina L. Impact of heat treatment on mechanical behaviour of Inconel 718 processed with tailored microstructure by selective laser melting. Mater Des. 2017;131:12–22. https://doi.org/10.1016/j.matdes.2017.05.065.
41. Tinoco J, Fredriksson H. Solidification of a modified inconel 625 alloy under different cooling rates. High Temp Mater Process. 2004;23:13–24. https://doi.org/10.1515/HTMP.2004.23.1.13.
42. Li C, White R, Fang XY, Weaver M, Guo YB. Microstructure evolution characteristics of Inconel 625 alloy from selective laser melting to heat treatment. Mater Sci Eng A. 2017;705:20–31. https://doi.org/10.1016/j.msea.2017.08.058.
43. Li S, Wei Q, Shi Y, Zhu Z, Zhang D. Microstructure characteristics of Inconel 625 superalloy manufactured by selective laser melting. J Mater Sci Technol. 2015;31:946–52. https://doi.org/10.1016/j.jmst.2014.09.020.
44. Marchese G, Aversa A, Bassini E. Microstructure and hardness evolution of solution annealed inconel 625/TiC composite processed by laser powder bed fusion. Metals (Basel). 2021;11:929. https://doi.org/10.3390/met11060929.
45. Kok Y, Tan XP, Wang P, Nai MLS, Loh NH, Liu E, Tor SB. Anisotropy and heterogeneity of microstructure and mechanical properties in metal additive manufacturing: a critical review. Mater Des. 2018;139:565–86. https://doi.org/10.1016/j.matdes.2017.11.021.
46. Sergueeva AV, Zhou J, Meacham BE, Branagan DJ. Gage length and sample size effect on measured properties during tensile testing. Mater Sci Eng A. 2009;526:79–83. https://doi.org/10.1016/j.msea.2009.07.046.
47. Marchese G, Lorusso M, Parizia S, Bassini E, Lee J-W, Calignano F, Manfredi D, Terner M, Hong H-U, Ugues D, Lombardi M, Biamino S. Influence of heat treatments on microstructure evolution and mechanical properties of Inconel 625 processed by laser powder bed fusion. Mater Sci Eng A. 2018;729:64–75. https://doi.org/10.1016/j.msea.2018.05.044.
48. Todaro CJ, Easton MA, Qiu D, Zhang D, Bermingham MJ, Lui EW, Brandt M, Stjohn DH, Qian M. Grain structure control during metal 3D printing by high-intensity ultrasound. Nat Commun. 2020. https://doi.org/10.1038/s41467-019-13874-z.
49. Oerlikon, Additive manufacturing 625 Nickel Alloy, 1900.
50. Sitek R, Molak R, Zdunek J, Bazarnik P, Wiśniewski P, Kubiak K, Mizera J. Influence of an aluminizing process on the microstructure and tensile strength of the nickel superalloy IN 718 produced by the selective laser melting. Vacuum. 2021;186: 110041. https://doi.org/10.1016/j.vacuum.2020.110041.
51. Szustecki M, Zrodowski L, Sitek R, Cygan R, Pakiela Z, Mizera J. Microstructure and properties of IN 718 nickel-based superalloy

manufactured by means of selective laser melting method. Adv Appl Plasma Sci. 2017;11:9–12.
52. Amato K, Hernandez J, Murr L, Martinez E, Gaytan S, Shindo P, Collins S. Comparison of microstructures and properties for a Ni-base superalloy (alloy 625) fabricated by electron beam melting. J Mater Sci Res. 2012;1(2):3. https://doi.org/10.5539/jmsr.v1n2p3.
53. Frankel GS. Pitting corrosion of metals: a review of the critical factors. J Electrochem Soc. 1998;145:2186–98. https://doi.org/10.1149/1.1838615.
54. Wong H, Dawson K, Ravi GA, Howlett L, Jones RO, Sutcliffe CJ. Multi-laser powder bed fusion benchmarking—initial trials with inconel 625. Int J Adv Manuf Technol. 2019;105:2891–906. https://doi.org/10.1007/s00170-019-04417-3.
55. Marchese G, Bassini E, Parizia S, Manfredi D, Ugues D, Lombardi M, Fino P, Biamino S. Role of the chemical homogenization on the microstructural and mechanical evolution of prolonged heat-treated laser powder bed fused Inconel 625. Mater Sci Eng A. 2020;796: 140007. https://doi.org/10.1016/j.msea.2020.140007.
56. Nguejio J, Szmytka F, Hallais S, Tanguy A, Nardone S, Godino-Martinez M. Comparison of microstructure features and mechanical properties for additive manufactured and wrought nickel alloys 625. Mater Sci Eng A. 2019;764:138214. https://doi.org/10.1016/j.msea.2019.138214.
57. Chen L, Sun Y, Li L, Ren X. Microstructural evolution and mechanical properties of selective laser melted a nickel-based superalloy after post treatment. Mater Sci Eng A. 2020;792: 139649. https://doi.org/10.1016/j.msea.2020.139649.